Observation of attosecond electron dynamics in the photoelectron momentum distribution of atoms using few-cycle laser pulses

Mitsuko Murakami* and Guo-Ping Zhang
Department of Physics, Indiana State University, Terre Haute, Indiana 47809, USA

(Received 4 March 2020; accepted 6 May 2020; published 28 May 2020)

The method of time-resolved measurement with ultrashort laser pulses is vital to the development of attosecond science. Pump-probe measurements using a train of attosecond pulses in combination with a near-infrared (NIR) multicycle driving laser have been successful in capturing the intercycle electron dynamics which repeats every optical cycle and leads to above-threshold ionization (ATI) spectra in the frequency domain. In this work, we study the effect of a carrier-envelope phase (CEP) in a few-cycle (<6 fs) NIR laser pulse on the photoelectron momentum distribution (PMD) of a hydrogen atom and show that interference patterns in a PMD change dramatically with CEPs in the few-cycle regime. When the few-cycle driving laser pulse has a sine shape, the double-slit interference with characteristic modulation of ATI peaks dominates the PMD. On the other hand, when the driving pulse has a cosine shape, the holographical interference featured by a spider-like pattern is isolated. Our results suggest that the CEP-stable few-cycle laser pulses can be used to identify different types of intracycle interference structures in a PMD which reveal the underlying subcycle electron dynamics on an attosecond timescale.

DOI: 10.1103/PhysRevA.101.053439

I. INTRODUCTION

Velocity map imaging (VMI) is a powerful technique to measure electron dynamics driven by a strong laser field [1]. Combined with reaction microscopes, VMI is capable of recording the three-dimensional momentum vector of photoionized electrons with a momentum resolution within a few percent of an atomic unit [2]. Moreover, development of femtosecond laser pulses with a stable carrier-envelope phase (CEP) has enabled, among other things, the generation of attosecond (<1 fs) laser pulses for pump-probe experiments [3]. By combining a multicycle, near-infrared (NIR) laser pulse and a train of attosecond, extreme ultraviolet (XUV) laser pulses in coincidence, VMI can record the motion of a three-dimensional photoelectron momentum distribution (PMD) during the photoionization of atoms in a stroboscopic manner, with the time resolution of a few femtoseconds [4,5]. This method, however, is only sensitive to a particular type of photoelectron motions that repeats every optical cycle of the NIR laser, i.e., intercycle dynamics. Another approach to the time-resolved VMI is to use the CEP-stabilized few-cycle NIR laser pulses directly [6]. In the few-cycle regime, electron dynamics recorded in PMDs are extremely sensitive to and even controlled by the CEP [7]. Although there are numerous studies on PMD driven by few-cycle laser pulses in recent years [8–13], effects of CEPs have not been discussed extensively, particularly in terms of their use in attosecond physics.

The information of electron dynamics is recorded in a PMD as various forms of interferometric patterns [14]. Similar to optical interferometry where light is split into two beams and follows different optical paths before being recombined, the interference in a PMD is caused by two photoelectron wave packets that arrive at a detector with the same final momentum but different phases. Their phase difference reflects the separate quantum paths they follow after being photoionized from a parent ion before arriving at the detector [15]. There are a number of possible pairs of quantum paths that coherently interfere at the detector, and they produce different interference patterns [16–18]. Broadly speaking, they are classified into intra- and intercycle interferences, depending on whether or not the two interfering wave packets are released from the parent ion within the same optical cycle of a driving laser field. Since the driving laser field is a periodic function of time, electron wave packets which are released with exactly one optical-cycle time delays in between follow the same drifting motion and constructively interfere at the detector. Because it is a cycle-to-cycle interference, it is referred to as intercycle interference. Intracycle interferences are less trivial because electron wave packets must follow different paths but still coherently interfere. In the multicycle regime, both intra- and intercycle interferences are possible, and the CEP does not influence the PMD. As a result, the PMD driven by multicycle lasers exhibits more than one type of interference patterns, which obstruct one another. A few-cycle driving laser pulse assures that only intracycle interference appears in a PMD.

A potential area of research where the CEP of a few-cycle driving laser could be useful is strong-field photoelectron holography [8]. It was discovered in 2011 by using long-wavelength (7 μm) laser pulses from a free-electron laser and has interference minima and maxima spreading in the radial direction (often described as spider legs in the literature) [16]. The long wavelength was thought to be crucial for the observation of this spider-like interference [19], but it was later

*mitsuko.murakami@indstate.edu

observed with NIR lasers (≈800 nm) as well [20,21]. This type of intracycle interference originates from two electron wave packets born within the same quarter cycle of a driving laser pulse [10,16–18]. It is assumed that one of them (referred to as the signal) rescatters with their parent ion and encodes its temporal and structural information, while the other (referred to as the reference) does not; because their interference structure can then be considered as a photoelectron holography of the parent ion, the spider-like pattern is said to be holographic by nature. As we demonstrate in this paper, the CEP of a few-cycle driving laser is particularly useful in isolating the spider-like interference in PMDs.

Very recently, an alternative explanation for the spider-like interference structure in a PMD was proposed [22]. It claims that the spider-like pattern in a PMD is an optical glory caused by the electron wave packets that is reflected by a parent ion. We use the word "reflected" rather than "rescattered" since an electron trajectory for the glory interference is midway between the direct and rescattering electrons which cause the spider-like pattern [13]. This theory may seem more plausible than the conventional holography explanation discussed above for the following reason: It is well known from the study of above-threshold ionization (ATI) that the energy of the electrons which reach the detector directly without rescattering with their parent ions do not exceed $2U_p$, where $U_p = I_0/4\omega_0{}^2$ is the ponderomotive energy of a driving laser field of peak intensity I_0 and frequency ω_0 [23]. The majority of electrons reach the detector directly, without rescattering with their parent ions, so that the intensity of ATI spectra falls off drastically at $2U_p$. The energy of rescattered electrons, on the other hand, could reach $10U_p$, but their spectral intensity is several orders of magnitude smaller than that of direct electrons [24]. Knowing their huge difference in photoelectron intensity, it is not obvious how the direct and the rescattered electron wave packets could coherently interfere in a PMD. The optical glory is caused by reflected electrons of similar photoelectron intensities and thus should be observable at photoelectron energies below $2U_p$. The nature of spider-like interference is still debatable at the moment.

In this work, we study the intracycle interference structures in a PMD of a H (hydrogen) atom by using a few-cycle (<6 fs) strong driving laser pulse. We find that the interference patterns in a PMD change dramatically with CEPs. Specifically, the CEP-stabilized few-cycle laser pulses allow us to evaluate the location of electron-density maxima associated with double-slit interferences [25], or to isolate the spider-like pattern which is a type of holographic interference [16,21]. In addition, a new type of holographical interference (described as boomerang-like in Ref. [13]) becomes visible with the CEP-stabilized few-cycle driving laser pulses. The fact that CEPs reveal these different interference patterns in a PMD means that the CEP controls the intracycle electron dynamics on an attosecond timescale.

The paper is organized as follows: In Sec. II, we briefly discuss the theoretical methods of our calculation based on the numerical solutions of the time-dependent Schrödinger equation (TDSE). Then, in Secs. III A and III B, we present our results when the CEP of few-cycle driving laser pulses is set to zero (i.e., the laser electric field is sine-like) and $\pi/2$ (cosine-like), respectively, followed by the conclusion in Sec. IV. Atomic units ($e = m_e = \hbar = 1$) are used throughout unless specified otherwise.

II. METHODS

We solve the time-dependent Schrödinger equation (TDSE) in the length gauge for an electron of a H atom driven by a strong laser field in the limit of the dipole approximation, which is given by

$$i\frac{\partial}{\partial t}\psi_{i\sigma}(\mathbf{r},t) = \left[\frac{-1}{2}\nabla^2 - \frac{1}{r} + \mathbf{E}(t)\cdot\mathbf{r}\right]\psi_{i\sigma}(\mathbf{r},t), \tag{1}$$

by using the generalized pseudospectral (GPS) method [26]. The numerical details of our calculation are given in Ref. [27]. For the results of this paper, the driving laser field $\mathbf{E}(t)$ is linearly polarized along the z axis, i.e.,

$$\mathbf{E}(t) = E_0(t)\sin(\omega_0 t + \phi)\hat{\mathbf{z}}, \tag{2}$$

where ω_0 is the laser frequency, ϕ is the CEP, and $E_0(t)$ is the envelope function centered around $t = 0$ and given by

$$E_0(t) = \sqrt{I_0}\cos^2\left(\frac{\omega_0 t}{2n}\right), \tag{3}$$

with n being the number of cycles per pulse. In this work, we let $n = 2$ to ensure that the intercycle interference does not appear in a PMD [12]. The linearly polarized driving laser field (2) makes the laser potential in Eq. (1) azimuthally symmetric, so the problem is two dimensional (2D).

The solution of the TDSE is split into the inner and the outer regions at each time step by an absorbing function $f(r)$ that is unity in the inner region ($0 < r \leqslant R_b$) and zero in the outer region ($R_b < r \leqslant r_{\max}$), as follows:

$$\begin{aligned}\psi(\mathbf{r},t) &= f(r)\psi(\mathbf{r},t) + [1 - f(r)]\psi(\mathbf{r},t)\\ &= \psi_{(\mathrm{in})}(\mathbf{r},t) + \psi_{(\mathrm{out})}(\mathbf{r},t).\end{aligned} \tag{4}$$

Then, the outer wave function is propagated in momentum space with the Volkov Hamiltonian in the velocity gauge [15,28]; that is,

$$\psi_\infty(\mathbf{p},t+\Delta t) = e^{-i\mathcal{H}^v_\infty(t)\Delta t}\left[\psi_\infty(\mathbf{p},t) + \tilde{\psi}^v_{(\mathrm{out})}(\mathbf{p},t)\right], \tag{5}$$

where $\mathcal{H}^v_\infty = [\mathbf{p} + \mathbf{A}(t)]^2/2$ is the Volkov Hamiltonian for a vector potential $\mathbf{A}(t) = -\int_{-\infty}^{t}\mathbf{E}(t')dt'$, and $\tilde{\psi}^v_{(\mathrm{out})}(\mathbf{p},t)$ is the Fourier transform of the outer wave function $\psi_{(\mathrm{out})}(\mathbf{r},t)$ in the velocity gauge, i.e.,

$$\psi^v_{(\mathrm{out})}(\mathbf{r},t) = e^{i\mathbf{A}(t)x}\psi_{(\mathrm{out})}(\mathbf{r},t). \tag{6}$$

Note that $\psi_\infty(\mathbf{p},-\infty) = 0$ initially, as long as a sufficiently large boundary R_b is chosen.

At the end of a few-cycle driving laser pulse, the time evolution is continued for two more empty optical cycles to allow some time for relaxations. Then, the PMD is obtained by taking a cross section along the p_z axis of a density distribution $D(\mathbf{p})$ in the outer region; that is,

$$D(\mathbf{p}) = |\psi_\infty(\mathbf{p},\infty)|^2. \tag{7}$$

In practice, the solution to TDSE for an electron in a linearly polarized laser is a 2D function of radial distance r and polar angle θ, or of their canonical conjugates p and θ_p, which is what we mean by the "cross section." If we rotate its

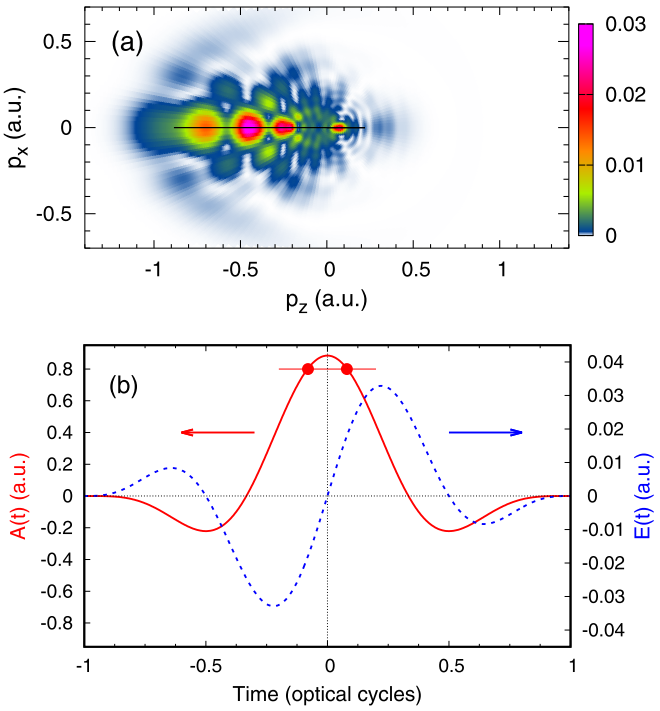

FIG. 1. (a) Photoelectron momentum distribution (PMD) of a H atom, driven by a monochromatic (800 nm), linearly polarized two-cycle driving laser pulse of a peak intensity $I_0 = 5 \times 10^{13}$ W/cm^2 and a carrier-envelope phase (CEP) $\phi = 0$. A series of pronounced maxima in electron density, characteristic of the double-slit interference, appears along the polarization axis p_z of a driving laser potential. Also shown with a black line is the classical path of an electron: $\mathbf{p} = -\mathbf{A}(t)$. (b) Electric-field strength $\mathbf{E}(t)$ (dotted line) and its corresponding vector potential $\mathbf{A}(t)$ (solid line) used to obtain the PMD in Fig. 1(a). For the 800 nm laser field, one optical cycle corresponds to 2.67 fs. For illustrative purposes, the time gating of two degenerate electron wave packets is indicated with a pair of closed circles on the $\mathbf{A}(t)$ graph. They coherently interfere at the detector only if the corresponding field strengths $\mathbf{E}(t)$ at the time of their ionization have the same magnitude but opposite direction, as is the case in this figure.

density distribution around the p_z axis, we would obtain the complete three-dimensional PMD. In our paper, we plot an extended range of $\theta \in [0, 2\pi]$ rather than $\theta \in [0, \pi]$ in the same way as the measured PMDs. (What is actually measured in experiments is the projection of the electron distribution onto a plane at the detector, but the cross-sectional distribution is obtained by taking its Abel transform.)

III. RESULTS

A. Few-cycle driving laser with carrier-envelope phase = 0

Figure 1(a) shows the PMD of a H atom driven by an 800 nm, two-cycle driving laser pulse of peak intensity $I_0 = 5 \times 10^{13}$ W/cm^2, when its CEP of Eq. (2) is $\phi = 0$. To describe the specific effect of CEP on electron dynamics, we plot in Fig. 1(b) the electric-field strength $\mathbf{E}(t)$ of the driving laser pulse and its corresponding vector potential $\mathbf{A}(t)$ used in the calculation of Fig. 1(a). When $\phi = 0$, the vector potential (solid line) is symmetric with respect to the pulse peak. A pair of solid circles on $\mathbf{A}(t)$ indicate two identical field amplitudes around the pulse peak.

The intercycle interference, which is known to cause concentric peaks that are spaced by one photon energy and centered at the origin of a PMD [29], is absent due to the short duration of the driving laser pulse. On the other hand, the near-threshold interference, characterized by a petal-shaped interference close to the origin of a PMD [30–34], is expected to appear below the momentum of the lowest-order above-threshold electron, given by [35,36]

$$p = \sqrt{2[(n_\infty + 1)\omega_0 - (I_p + U_p)]}, \tag{8}$$

where n_∞ is the number of photons absorbed to reach the nearest-threshold Rydberg state; namely,

$$n_\infty = \lfloor (I_p + U_p)/\omega_0 \rfloor, \tag{9}$$

in which the symbol $\lfloor x \rfloor$ denotes the floor function, i.e., the largest integer smaller than x. The upshift of the ionization energy I_p by the ponderomotive energy U_p of a laser field is implied in Eq. (8), which can be derived by using the time-dependent perturbation theory [27]. For the driving laser in Fig. 1(a), $n_\infty = 10$, and Eq. (8) gives $p = 0.18$ a.u., which affects a very small region of the PMD in Fig. 1(a). The interference patterns in Fig. 1(a) must therefore come from a different type of electron dynamics.

The classical equation of motion of an electron in a laser field according to the simple man's model [37] (i.e., neglecting the binding potential of an atom) is $\ddot{\mathbf{r}} = -\mathbf{E}(t)$. The corresponding equation of its momentum vector is $\mathbf{p}(t) = \mathbf{p}_\infty + \mathbf{A}(t)$, where $\mathbf{A}(t) = -\int_{-\infty}^{t} \mathbf{E}(t')dt'$ is the vector potential. Since $\mathbf{A}(t = \infty) = 0$, we find that $\mathbf{p}(t = \infty) = \mathbf{p}_\infty$ is the asymptotic momentum measured at the detector. If we further assume that the initial momentum of the electron is zero at the time t_i of ionization, then $\mathbf{p}_\infty + \mathbf{A}(t_i) = 0$, or [38]

$$\mathbf{p}_\infty = -\mathbf{A}(t_i). \tag{10}$$

Therefore, classical paths of an electron in momentum space are twofold degenerate per optical cycle when the vector potential $\mathbf{A}(t)$ is the same, as indicated with the pair of closed circles in Fig. 1(b). Because of the short duration of a driving laser, a positive half cycle of $\mathbf{A}(t)$ in Fig. 1(b) is centered around the pulse peak, but negative half cycles of $\mathbf{A}(t)$ before and after the peak are suppressed by the pulse envelope, causing an electron to rescatter from the nucleus mostly from the negative z direction. In other words, if $\mathbf{A}$(t) is mostly positive, as shown in Fig. 1(b), then the electron density in a PMD should appear in the negative-z region of a PMD, as shown in Fig. 1(a). Moreover, because the CEP $\phi = 0$ makes $\mathbf{E}(t)$ an odd function of time, those degenerate electron wave packets in Fig. 1(b) are born when the electric field $\mathbf{E}(t)$ has the same magnitude but in the opposite directions; this is in fact a condition for the double-slit interference, which was first measured in Ref. [39] by using few-cycle driving laser pulses and later angularly resolved in Ref. [40]. This type of interference is due to electron dynamics along the laser polarization axis, which is essentially one dimensional [25]. Indeed, Fig. 1(a) shows prominent interference peaks along the negative-p_z axis.

When integrated over polar angles and expressed in terms of photoelectron energy ($p^2/2$), the intercycle interference in

a PMD yields well-known ATI spectra which are regularly spaced by one photon energy ($\hbar\omega_0$) [41,42]. The double-slit interference we find in Fig. 1(a), on the other hand, leads to photoelectron spectra whose separation increases with photoelectron energy [7,25]. In experiments using a multicycle driving laser pulse, the double-slit interference structure is less prominent than the intercycle interference and only appear as a height modulation between ATI peaks [39]. Yet, quantum calculations suggest that they become comparably strong in the deep tunneling regime where Keldysh parameter $\gamma = \sqrt{I_p/2U_p}$ is considerably less than 1 [43]. There is even a higher-order effect which is caused by the superposition of the intercycle and the double-slit interference; the resulting interference pattern in a PMD is featured by concentric rings whose origin is shifted by an amount of $\pm\sqrt{2(2U_p)}$ along the axis of a driving vector potential [43]. Because we use the few-cycle driving laser pulse, the higher-order effect (between inter- and intracycle interferences) does not appear in Fig. 1(a).

Furthermore, we also observe in Fig. 1(a) an appearance of holographical interference which spreads in the shape of spider legs [16]. The spider-like interference in Fig. 1(a) appears only in the negative-p_z side of the PMD, and its photoelectron intensity is not as strong as the double-slit interference which concentrates along the laser polarization axis. Interestingly, it is modulated not only along the p_z axis (due to the double-slit interference) but also along its spider legs, and the locations of extrema along the spider legs are down-shifted in photoelectron energy compared with those along the p_z axis. This is because yet another type of interference structure intersects the spider-like interference. Ref. [13] calls it the type-I boomerang-like interference, which appears as v-shaped stripes in a PMD whose pointy side faces the origin of a PMD and repeats along the polarization axis of a vector potential. The fact that its convex side faces the origin suggests that it is caused by incoming wave packets. It is a nonholographic interference between the two nonscattering (direct) electrons released during the first half cycle and those during the second half cycle. The spider-like pattern, on the other hand, is due to two electron wave packets released within the same quarter optical cycle of a driving laser field [10,16–18]. A careful observation of Fig. 1(a) further reveals yet another boomerang-like interference structure above the ATI cutoff ($\sqrt{2(2U_p)} = 0.66$ a.u.) whose pointy side faces away from the origin; it is called the type-II boomerang-like interference in Ref. [13] and is another type of holographical interference between the electron which is ionized in the first half-cycle of a driving laser pulse and rescatters with a parent ion within a half optical-cycle (so-called the short-trajectory rescattering) and the direct electron ionized in the next half-cycle.

As we increase the peak intensity while keeping the rest of the parameters of the two-cycle laser pulse used in Fig. 1(a), the double-slit interference patterns along the p_z axis extend to higher momenta, which is shown in Fig. 2. In Fig. 3, we plot the corresponding photoelectron spectra for three different peak intensities, which are obtained by integrating PMDs in Figs. 1(a) and 2 over polar angles. The modulation of ATI peaks and the characteristic feature of double-slit interference described in Ref. [25] (akin to the modulation of Bragg peaks in crystal diffraction by internal structure within the unit cell) are clearly visible in Fig. 3, but the down-shifted interference peaks along the spider legs observed in Figs. 1(a) and 2 tend to raise the interference minima of double-slit interference far from zero.

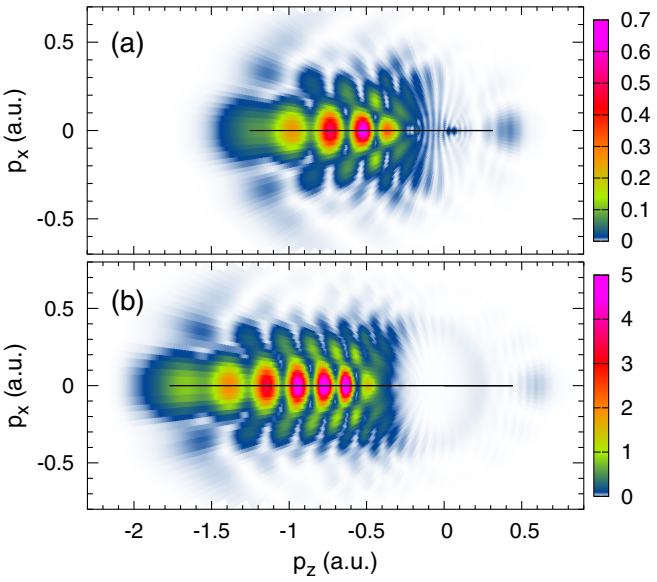

FIG. 2. The same as Fig. 1(a), but the peak intensity of a driving laser is increased to (a) $I_0 = 1 \times 10^{14}$ W/cm^2 and (b) $I_0 = 2 \times 10^{14}$ W/cm^2. Also shown with a black line in each plot is the classical path of an electron: $\mathbf{p} = -\mathbf{A}(t)$.

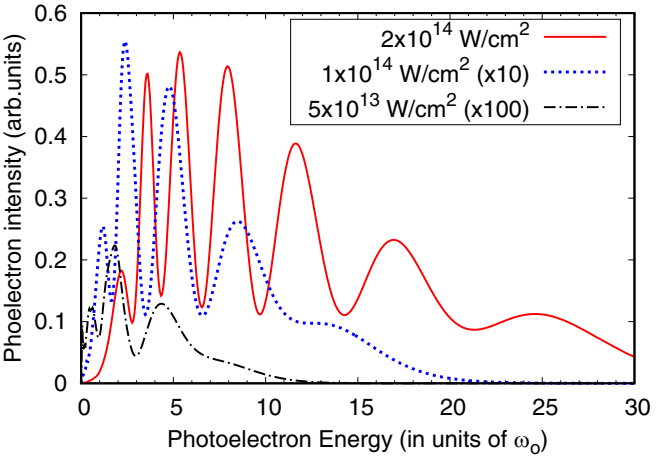

FIG. 3. Above-threshold ionization (ATI) spectra of a H atom, driven by a monochromatic (800 nm), linearly polarized 2-cycle driving laser pulse of a carrier-envelope phase $\phi = 0$ for three different peak intensities: $I_0 = 5 \times 10^{13}$, 1×10^{14}, and 2×10^{14} W/cm^2. They are obtained by integrating the PMDs in Figs. 1(a) and 2 over polar angles and expressing them as functions of photoelectron energy ($p^2/2$). For clarity, the photoelectron yield for lower peak-intensity calculations are multiplied by 10 and 100. Notice that these spectra do not follow the conventional multicycle ATI interference patterns (i.e., equispaced by one-photon transition energy $\hbar\omega_0$) but rather increase their separations with energy, which is a characteristic of intracycle interference.

Another interesting observation we can make from Fig. 2 is that there is a region near the origin of a PMD in Fig. 2(b) where electron population vanishes. For lower peak-intensity calculations in Fig. 1(a), such a region is absent, and therefore this behavior may be associated more with the tunneling ionization regime ($\gamma \ll 1$) than with the multiphoton ionization regime ($\gamma \approx 1$). The lowest momentum for above-threshold ionization given by Eq. (8) is $p = 0.20$ a.u. for Fig. 2(a) and 0.24 a.u. for Fig. 2(b) (with $n_\infty = 12$ and 16, respectively), and the absence of interference in a PMD below these radii could therefore imply tunneling ionization. On the contrary, many studies using multicycle driving lasers show that the near-threshold interference structure characterized by its petal-like shape appears in the near-zero-momentum region no matter what the tunneling or multiphoton ionization regime [29,30,32,33,36]. It is generally understood that the near-threshold interference is visible regardless of the intensity or the frequency of a driving-laser pulse, as long as it is linearly polarized and its photon energy ($\hbar\omega_0$) does not exceed the ionization energy [34]. Its disappearance in Fig. 2(b) is therefore quite surprising.

In fact, according to the virial theorem, the deeply bound electron has much higher kinetic energy than the near-threshold electron. The tunnel-ionized electron could therefore have large kinetic energy when entering the tunneling barrier. The tunneling exit is defined as the point where the kinetic energy is zero, but the initial momentum of an electron at a specific position is not a definite quantity in quantum mechanics. Reference [44] defines the longitudinal momentum of a photoionized electron at the tunneling exit as the flow momentum of the probability fluid and shows that it can be substantial (estimated to be around 0.2 a.u.) in the nonadiabatic regime. If this is the case, then the tunnel-ionized photoelectron would appear at larger radius in a PMD than predicted by Eq. (8). Our finding is supported by Fig. 3 of Ref. [43], where they manually extract the electron wave packets from two different quarter cycles of a multicycle driving laser field by time windowing, effectively limiting the duration of electron dynamics to be a few optical cycles. The resulting PMDs in the near-zero-momentum region of Ref. [43] are empty in the tunneling regime, similar to our Fig. 2(b). There must be a mechanism associated with the short duration of a driving laser pulse which prevents the near-threshold interference. One possible explanation is that the duration of a few-cycle driving laser pulse is too short for the tunnel-ionized electron wave packets to rescatter with a parent ion and induce the near-threshold interference in a PMD. It is analogous to the fact that the petal-like interference structure characteristic to near-threshold ionization is absent in a PMD if driven by a circularly polarized laser which causes no rescattering [27,45].

B. Few-cycle driving laser with carrier-envelope phase = $\pi/2$

Next, we consider when the CEP of $\mathbf{E}(t)$ is $\phi = \pi/2$, as shown in Fig. 4. The PMD shown in Fig. 4(a) is dramatically different from Fig. 1(a), although all the laser parameters used for these two figures are the same except for the CEP. The only structure which appears in Fig. 4(a) is the spider-like interference. Aside from one strong peak which lies along the positive-p_z axis, the PMD in Fig. 4(a) peaks along several parabolic curves whose convex sides all face to the left of the figure. There is essentially no other interference structure in Fig. 4(a), suggesting that all the other intracycle interferences we discussed in the last section are subsidiary in this case. What is also remarkable is the fact that a few-cycle driving laser pulse makes the spider-like interference clearly visible even though it has a NIR laser wavelength (800 nm). With multicycle driving laser pulses, the spider-like interference is hard to observe unless longer wavelengths (1200–1600 nm) are used [19].

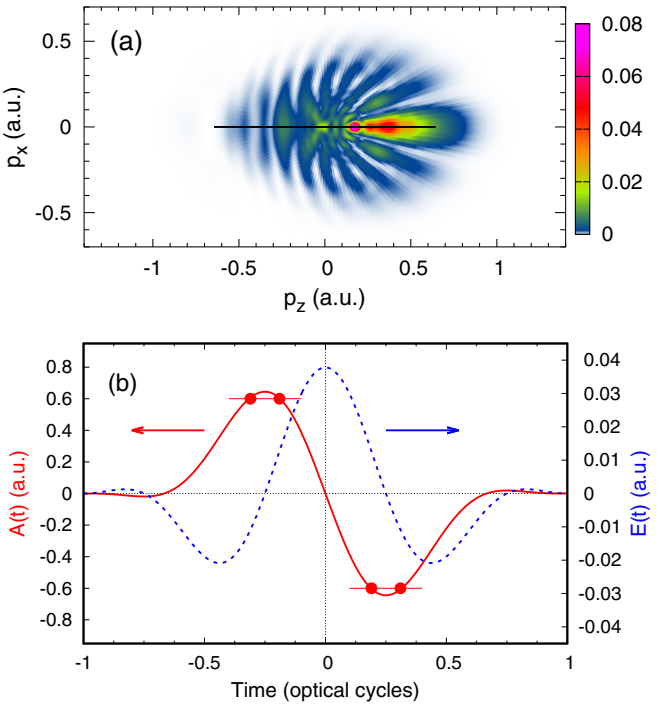

FIG. 4. (a) Photoelectron momentum distribution (PMD) of a H atom, driven by a monochromatic (800 nm), linearly polarized two-cycle driving laser pulse of a peak intensity $I_0 = 5 \times 10^{13}$ W/cm^2 and a carrier-envelope phase (CEP) $\phi = \pi/2$. (b) Electric-field strength $\mathbf{E}(t)$ (dotted line) and its corresponding vector potential $\mathbf{A}(t)$ (solid line) used to obtain the PMD in Fig. 4(a). The time gating for double-slit interference [indicated with a pair of closed circles in each negative or positive side of on the $\mathbf{A}(t)$ graph in panel (b)] does not produce coherent electron wave packets in this case because the field strengths $\mathbf{E}(t)$ at the time of their ionization do not have same magnitude. As a result, the spider-like interference is isolated in panel (a).

Figure 4(b) shows that the vector potential $\mathbf{A}(t)$ used for Fig. 4(a) is an odd function of time; that is, positive and negative half cycles of $\mathbf{A}(t)$ have equally strong amplitude around $t = 0$, so that electrons could in principle ionize into both directions. The PMD in Fig. 4(a) is nevertheless asymmetric, whose electron population is largely concentrating in the positive-p_z side of the PMD. This is a causal effect of the driving laser field; i,e., the electron tends to ionize more after the peak of the driving laser pulse than before. To show this, we plot in Fig. 5 the ionization probability and the ionization rate of a H atom driven by an 800 nm, linearly polarized, two-cycle driving laser pulse of peak intensity $I_0 =$

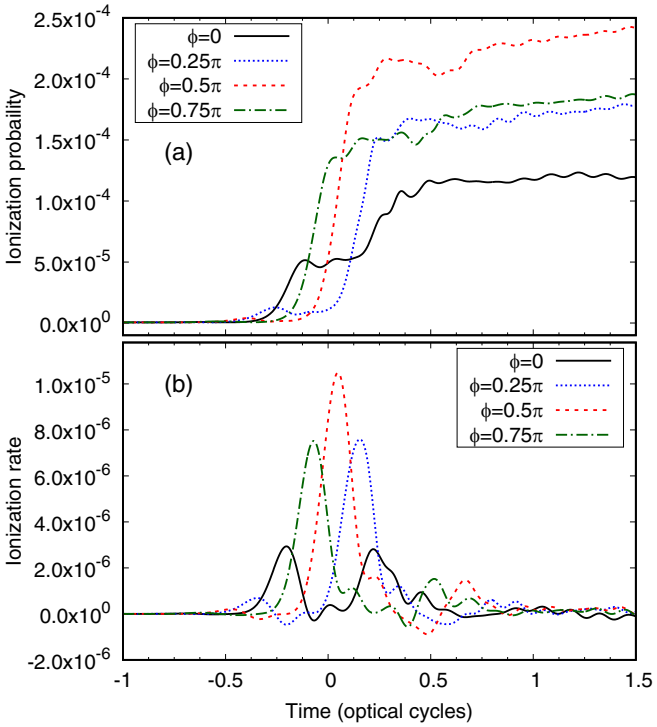

FIG. 5. (a) The ionization probability of a H atom during the interaction with the monochromatic (800 nm), linearly polarized two-cycle driving laser pulse of a peak intensity $I_0 = 5 \times 10^{13}$ W/cm^2 and various CEPs. (b) The time derivative of Fig. 5(a), after application of a low-pass Butterworth filter with cutoff frequency of 5 cycle^{-1}.

5×10^{13} W/cm^2 for various CEPs. The ionization probability in Fig. 5(a) is evaluated as the electron density outside the radius of $r = 10$, and the ionization rate in Fig. 5(b) is obtained by taking the time derivative of the ionization probability after an application of a low-pass Butterworth filter. We find that the majority of the ionization when $\phi = \pi/2$ takes place near the pulse peak at $t = 0$. The vector potential peaks in the negative direction after $t = 0$, so the electron dynamics after the pulse peak takes place in the positive-p_z direction [because $\mathbf{p}_\infty = -\mathbf{A}(t_i)$]. There is a pair of degenerate electron paths in each positive- or negative-p_z direction when the CEP is $\phi = \pi/2$, as indicated with two pairs of closed circles in Fig. 4(b). However, they do not coherently interfere because, unlike in Fig. 1(b) when $\phi = 0$, the magnitude of $\mathbf{E}(t)$ at the time of their release is different, which is why the double-slit interference is absent in Fig. 4(a).

In Fig. 6 we plot the PMDs that are calculated with the same CEP ($\phi = \pi/2$) but higher peak intensities of a driving laser than in Fig. 4. The spider-like interference appears only in the positive-p_z side of these PMDs, indicating that electron wave packets are rescattering from the negative side of a parent ion. There is a sizable amount of electron population in the negative-p_z side of PMDs in Fig. 6, but they do not show spider-like interference, which means that they are released before the pulse peak when $\mathbf{A}(t)$ is positive and directly ionized to the negative side of a driving laser axis without rescattering. Similarly to Fig. 2(b) in the previous section, we

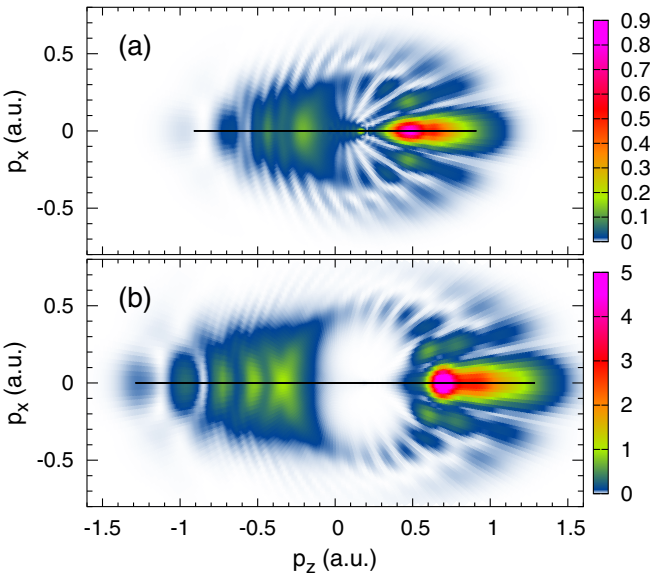

FIG. 6. The same as Fig. 4(a) but the peak intensity of a driving laser is increased to (a) $I_0 = 1 \times 10^{14}$ W/cm^2 and (b) $I_0 = 2 \times 10^{14}$ W/cm^2. Also shown with a black line in each plot is the classical path of an electron: $\vec{p} = -\vec{A}(t)$.

observe an empty region near the origin of a PMD in Fig. 6(b), possibly due to tunneling ionization.

Comparisons of Figs. 4(a) and 6 show that the number of spider legs do not change with the peak intensity of the driving laser, consistent with the findings of Ref. [9]. It does change, however, when the driving-laser wavelength is varied, which is shown in Fig. 7 where we use different driving-laser wavelengths (600 and 1200 nm). We find that the decrease in the frequency of a driving laser pulse causes an increase in the number of spider legs. To elaborate this point, we plot in Fig. 8 the photoelectron intensity as a function of polar angles alone,

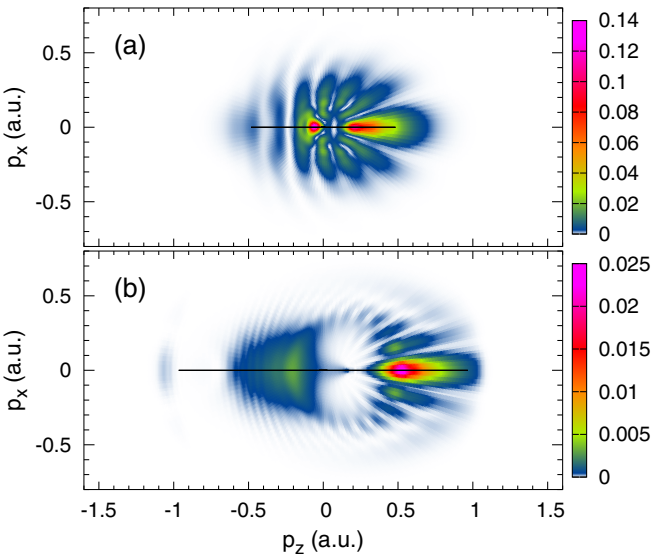

FIG. 7. The same as Fig. 4(a), but the wavelength of a driving laser is changed to (a) 600 nm and (b) 1200 nm.

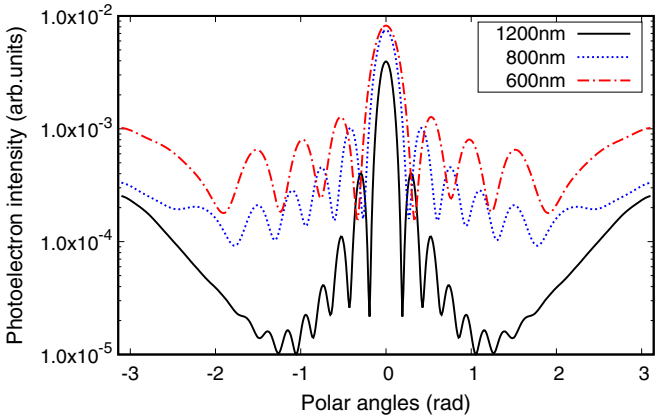

FIG. 8. Radially integrated photoelectron momentum distribution (PMD) of a H atom as a function of polar angles, driven by a linearly polarized two-cycle driving laser pulse of the peak intensity 5×10^{13} W/cm^2 and the carrier-envelope phase $\phi = \pi/2$ with three different wavelengths: 600, 800, and 1200 nm. The corresponding PMDs are given in Figs. 4(a) and 7.

which are obtained by integrating the radial variable out of the PMDs in Figs. 4(a) and 7. They show that the number of spider legs increases (whereas the separation of interference extrema decreases) for longer wavelengths of the driving laser, also consistent with Ref. [9]. The location of holographic fringes depends on the phase difference between the direct and the rescattering electron wave packets. Further investigation is needed to understand why the driving-laser frequency affects the phase difference. In addition to their phase, which is equal to the classical action of an electron in the field of a plane electromagnetic wave [16,17], one needs to account for the phase of their scattering amplitude, which increases with the scattering angle [46,47]. It should be emphasized that such a clear observation of the spider-like interference as in Fig. 8 is not possible with multicycle driving lasers because other types of interferences would also appear in a PMD. In Ref. [13], authors artificially switch off the ionization during the second half-cycle of a driving laser by projecting the wave function at the middle of a single-cycle driving laser pulse, in order to isolate the spider-like interference. Such a scheme is not possible experimentally, but the same effect can be achieved by a stabilized CEP in few-cycle driving laser pulses, as demonstrated in this work.

IV. CONCLUSION

Our systematic study of H-atom PMD driven by a few-cycle driving laser pulse with various CEPs has shown that the CEP is useful in isolating different intracycle interferences in a PMD to identify the underlying electron dynamics on an attosecond timescale. Similar results can be found in Ref. [48], in which PMDs of helium atoms were measured using a multicycle, two-color (790 nm + 345 nm) linearly polarized driving laser pulse. Our results show that the same effect is achieved by monochromatic few-cycle laser pulses with a stable CEP. The boomerang-like interference predicted in Ref. [13] but yet to been measured experimentally should also be observable with a CEP-stabilized few-cycle driving laser pulse. The angle-resolved measurements are desirable because the angle-averaged measurements (e.g., Ref. [49]) undermine the detailed interference structures in a PMD that are keys to the identification of intricate intracycle electron dynamics. In general, pulse durations of a laser beam are varied by increasing the pressure of the noble-gas medium within a hollow-core fiber, which induces the spectral broadening, thereby decreasing the Fourier-transform-limited pulse duration. The spectral phase introduced by the noble-gas media is compensated by a negative chirp created by chirped mirrors which prevents the dispersion in the remaining beam paths. Real-time, shot-by-shot measurements of the duration and the CEP of intense ($\approx 10 \times 14$ W/cm^2), few-cycle (4–10 fs), NIR (750–790 nm) laser pulses have already been reported in Refs. [50,51]. To accumulate enough photoelectron counts for velocity-map imaging (VMI), however, a prolonged measurement time would be required, during which CEP stabilization in every shot is essential. Spatial deviation of the CEP in the focal volume of ultrashort pulsed Gaussian beams can be managed by using a quasi-achromatic doublet lens [52]. It is our hope that such experiments become available in the future to promote a better understanding of the intracycle interferences.

ACKNOWLEDGMENTS

This work was supported by the U.S. Department of Energy under Contract No. DE-FG02-06ER46304. Numerical calculation was done on Indiana State University's quantum cluster and high-performance computer (obsidian). The research used resources of the National Energy Research Scientific Computing Center, which is supported by the Office of Science of the U.S. Department of Energy under Contract No. DE-AC02-05CH11231.

[1] G. P. Zhang, H. P. Zhu, Y. H. Bai, J. Bonacum, X. S. Wu, and T. F. George, Int. J. Mod. Phys. B **29**, 1550115 (2015).

[2] J. Ullrich, R. Moshammer, A. Dorn, R. Dörner, L. P. H. Schmidt, and H. Schmidt-Böcking, Rep. Prog. Phys. **66**, 1463 (2003).

[3] M. Hentschel, R. Kienberger, C. Spielmann, G. A. Reider, N. Milosevic, T. Brabec, P. Corkum, U. Heinzmann, M. Drescher, and F. Krausz, Nature (London) **414**, 509 (2001).

[4] J. Mauritsson, P. Johnsson, E. Mansten, M. Swoboda, T. Ruchon, A. L'Huillier, and K. J. Schafer, Phys. Rev. Lett. **100**, 073003 (2008).

[5] D. M. Villeneuve, P. Hockett, M. J. J. Vrakking, and H. Niikura, Science **356**, 1150 (2017).

[6] M. Kübel, Z. Dube, A. Y. Naumov, M. Spanner, G. G. Paulus, M. F. Kling, D. M. Villeneuve, P. B. Corkum, and A. Staudte, Phys. Rev. Lett. **119**, 183201 (2017).

[7] D. G. Arbó, E. Persson, and J. Burgdörfer, Phys. Rev. A **74**, 063407 (2006).

[8] M. Spanner, O. Smirnova, P. B. Corkum, and M. Y. Ivanov, J. Phys. B: At., Mol. Opt. Phys. **37**, L243 (2004).

[9] Y. Huismans, A. Gijsbertsen, A. S. Smolkowska, J. H. Jungmann, A. Rouzée, P. S. W. M. Logman, F. Lépine, C.

Cauchy, S. Zamith, T. Marchenko *et al.*, Phys. Rev. Lett. **109**, 013002 (2012).
[10] S. Borbély, A. Tóth, K. Tokési, and L. Nagy, Phys. Rev. A **87**, 013405 (2013).
[11] N. I. Shvetsov-Shilovski, M. Lein, L. B. Madsen, E. Räsänen, C. Lemell, J. Burgdörfer, D. G. Arbó, and K. Tokési, Phys. Rev. A **94**, 013415 (2016).
[12] S. Borbély, A. Tóth, D. G. Arbó, K. Tokési, and L. Nagy, Phys. Rev. A **99**, 013413 (2019).
[13] S. D. López and D. G. Arbó, Phys. Rev. A **100**, 023419 (2019).
[14] T. Remetter, P. Johnsson, J. Mauritsson, K. Varjú, Y. Ni, F. Epine, E. Gustafsson, M. Kling, J. Khan, R. López-Martens, K. Schafer, M. Vrakking, and A. L'Huillier, Nat. Phys. **2**, 323 (2006).
[15] M. Lein, J. P. Marangos, and P. L. Knight, Phys. Rev. A **66**, 051404(R) (2002).
[16] Y. Huismans, A. Rouzée, A. Gijsbertsen, J. H. Jungmann, A. S. Smolkowska, P. S. W. M. Logman, F. Lépine, C. Cauchy, S. Zamith, T. Marchenko *et al.*, Science **331**, 61 (2011).
[17] X.-B. Bian, Y. Huismans, O. Smirnova, K.-J. Yuan, M. J. J. Vrakking, and A. D. Bandrauk, Phys. Rev. A **84**, 043420 (2011).
[18] N. I. Shvetsov-Shilovski and M. Lein, Phys. Rev. A **97**, 013411 (2018).
[19] T. Marchenko, Y. Huismans, K. J. Schafer, and M. J. J. Vrakking, Phys. Rev. A **84**, 053427 (2011).
[20] S. G. Walt, N. Bhargava Ram, M. Atala, N. I. Shvetsov-Shilovski, A. von Conta, D. Baykusheva, M. Lein, and H. J. Wörner, Nat. Commun. **8**, 15651 (2017).
[21] G. Porat, G. Alon, S. Rozen, O. Pedatzur, M. Krüger, D. Azoury, A. Natan, G. Orenstein, B. D. Bruner, M. J. J. Vrakking, and N. Dudovich, Nat. Commun. **9**, 2805 (2018).
[22] Q. Z. Xia, J. F. Tao, J. Cai, L. B. Fu, and J. Liu, Phys. Rev. Lett. **121**, 143201 (2018).
[23] B. Walker, B. Sheehy, K. C. Kulander, and L. F. DiMauro, Phys. Rev. Lett. **77**, 5031 (1996).
[24] B. Sheehy, R. Lafon, M. Widmer, B. Walker, L. F. DiMauro, P. A. Agostini, and K. C. Kulander, Phys. Rev. A **58**, 3942 (1998).
[25] D. G. Arbó, K. L. Ishikawa, K. Schiessl, E. Persson, and J. Burgdörfer, Phys. Rev. A **81**, 021403(R) (2010).
[26] X.-M. Tong and S.-I. Chu, Chem. Phys. **217**, 119 (1997).
[27] M. Murakami and S.-I. Chu, Phys. Rev. A **93**, 023425 (2016).
[28] X. M. Tong, K. Hino, and N. Toshima, Phys. Rev. A **74**, 031405(R) (2006).
[29] D. A. Telnov and S.-I. Chu, Phys. Rev. A **79**, 043421 (2009).
[30] A. Rudenko, K. Zrost, C. D. Schröter, V. L. B. de Jesus, B. Feuerstein, R. Moshammer, and J. Ullrich, J. Phys. B: At., Mol. Opt. Phys. **37**, L407 (2004).
[31] C. M. Maharjan, A. S. Alnaser, I. Litvinyuk, P. Ranitovic, and C. L. Cocke, J. Phys. B: At., Mol. Opt. Phys. **39**, 1955 (2006).
[32] D. G. Arbó, S. Yoshida, E. Persson, K. I. Dimitriou, and J. Burgdörfer, Phys. Rev. Lett. **96**, 143003 (2006).
[33] M. Wickenhauser, X. M. Tong, D. G. Arbó, J. Burgdörfer, and C. D. Lin, Phys. Rev. A **74**, 041402(R) (2006).
[34] T. Marchenko, H. G. Muller, K. J. Schafer, and M. J. J. Vrakking, J. Phys. B: At., Mol. Opt. Phys. **43**, 095601 (2010).
[35] S. Basile, F. Trombetta, and G. Ferrante, Phys. Rev. Lett. **61**, 2435 (1988).
[36] Z. Chen, T. Morishita, A.-T. Le, M. Wickenhauser, X. M. Tong, and C. D. Lin, Phys. Rev. A **74**, 053405 (2006).
[37] P. B. Corkum, Phys. Rev. Lett. **71**, 1994 (1993).
[38] D. Würzler, N. Eicke, M. Möller, D. Seipt, A. M. Sayler, S. Fritzsche, M. Lein, and G. G. Paulus, J. Phys. B: At., Mol. Opt. Phys. **51**, 015001 (2017).
[39] F. Lindner, M. G. Schätzel, H. Walther, A. Baltuška, E. Goulielmakis, F. Krausz, D. B. Milošević, D. Bauer, W. Becker, and G. G. Paulus, Phys. Rev. Lett. **95**, 040401 (2005).
[40] R. Gopal, K. Simeonidis, R. Moshammer, T. Ergler, M. Dürr, M. Kurka, K.-U. Kühnel, S. Tschuch, C.-D. Schröter, D. Bauer *et al.*, Phys. Rev. Lett. **103**, 053001 (2009).
[41] K. J. Schafer and K. C. Kulander, Phys. Rev. A **42**, 5794 (1990).
[42] K. J. Schafer, B. Yang, L. F. DiMauro, and K. C. Kulander, Phys. Rev. Lett. **70**, 1599 (1993).
[43] W. Yang, H. Zhang, C. Lin, J. Xu, Z. Sheng, X. Song, S. Hu, and J. Chen, Phys. Rev. A **94**, 043419 (2016).
[44] R. Xu, T. Li, and X. Wang, Phys. Rev. A **98**, 053435 (2018).
[45] H. Xie, M. Li, S. Luo, Y. Li, Y. Zhou, W. Cao, and P. Lu, Phys. Rev. A **96**, 063421 (2017).
[46] Y. Zhou, O. I. Tolstikhin, and T. Morishita, Phys. Rev. Lett. **116**, 173001 (2016).
[47] M. He, Y. Li, Y. Zhou, M. Li, W. Cao, and P. Lu, Phys. Rev. Lett. **120**, 133204 (2018).
[48] X. Xie, S. Roither, D. Kartashov, E. Persson, D. G. Arbó, L. Zhang, S. Gräfe, M. S. Schöffler, J. Burgdörfer, A. Baltuška, and M. Kitzler, Phys. Rev. Lett. **108**, 193004 (2012).
[49] M. Kübel, M. Arbeiter, C. Burger, N. G. Kling, T. Pischke, R. Moshammer, T. Fennel, M. F. Kling, and B. Bergues, J. Phys. B: At., Mol. Opt. Phys. **51**, 134007 (2018).
[50] N. G. Johnson, O. Herrwerth, A. Wirth, S. De, I. Ben-Itzhak, M. Lezius, B. Bergues, M. F. Kling, A. Senftleben, C. D. Schröter *et al.*, Phys. Rev. A **83**, 013412 (2011).
[51] A. M. Sayler, T. Rathje, W. Müller, C. Kürbis, K. Rühle, G. Stibenz, and G. G. Paulus, Opt. Express **19**, 4464 (2011).
[52] M. A. Porras, Z. L. Horváth, and B. Major, Phys. Rev. A **98**, 063819 (2018).